Thermoelectric properties of nanocrystalline $(Mg_{1-x}Zn_x)_3Sb_2$ isostructural solid solutions fabricated by mechanical alloying

2009 J. Phys. D: Appl. Phys. 42 165403

(http://iopscience.iop.org/0022-3727/42/16/165403)

J. Phys. D: Appl. Phys. **42** (2009) 165403 (9pp) doi:10.1088/0022-3727/42/16/165403

Thermoelectric properties of nanocrystalline $(Mg_{1-x}Zn_x)_3Sb_2$ isostructural solid solutions fabricated by mechanical alloying

H X Xin, X Y Qin[1], J H Jia, C J Song, K X Zhang and J Zhang

Key Laboratory of Materials Physics, Institute of Solid State Physics, Chinese Academy of Science, 230031 Hefei, People's Republic of China

E-mail: xyqin@issp.ac.cn

Received 29 May 2009, in final form 30 June 2009
Published 31 July 2009
Online at stacks.iop.org/JPhysD/42/165403

Abstract

Mechanical alloying plus hot-pressing was employed to prepare nanocrystalline $(Mg_{1-x}Zn_x)_3Sb_2$ compounds that were characterized by microstructural examinations and dc electrical resistivity, Seebeck coefficient and thermal conductivity measurements. The results indicated that the grain size of $(Mg_{1-x}Zn_x)_3Sb_2$ compounds is ~30 nm; the structure and the transport properties can be tuned by isovalent Zn substitution for Mg in the tetrahedral positions for $(Mg_{1-x}Zn_x)_3Sb_2$ from $x = 0$ to ~0.6. It can be almost 90% concentration by replacing some of the Mg atoms in the tetrahedral position with Zn atoms in $(Mg_{1-x}Zn_x)_3Sb_2$. The distance between Mg–Sb decreases with increasing zinc content in $(Mg_{1-x}Zn_x)_3Sb_2$. The angle θ of Mg–Sb–Mg in the tetrahedral sites for $(Mg_{1-x}Zn_x)_3Sb_2$ changes non-monotonically with x. The electric transport behaviour changes because the Coulomb repulsion increases between Mg/Zn and Mg/Zn atoms in the tetrahedral position with the closer contact. The thermoelectric power factor (α^2/ρ) of $(Mg_{1-x}Zn_x)_3Sb_2$ for $x = 0.55$ (at 300 K) is more than 5×10^2 times larger than that of Mg_3Sb_2. Moreover, due to its extremely low thermal conductivity (~1.08 W m^{-1} K^{-1}), the dimensionless figure of merit, ZT, of $(Mg_{1-x}Zn_x)_3Sb_2$ with $x = 0.32$ is found to be over 80 times larger than that of Mg_3Sb_2 at 300 K.

1. Introduction

Magnesium antimonide compound is an important candidate for various functional (thermoelectricity [1], lithium battery [2], photoconduction [3], hydrogen transmitting [4] etc) and structural materials [5]. Mg_3Sb_2 has a hexagonal crystal structure of the anti-La_2O_3 type at room temperature, as shown in figure 1. The bonding characteristic of Mg_3Sb_2 should be between metallic and ionic [6, 7]. As in the case of the $CaAl_2Si_2$ structure, the stoichiometric Mg_3Sb_2 compound consists of interspersed $Mg_2Sb_2^{2-}$ layers (the tetrahedral position in the lattice) and Mg^{2+} cation layers (the octahedral position in the lattice) [8]. The interactions between the cations and the anionic layers are predominantly ionic and should contribute very little to the electronic conduction in which we are interested [9]. However, the ionic Madelung contribution is surely important in determining the stability of alternative structures [9]. Kajikawa *et al* performed an investigation of thermoelectric properties on Mg_3Sb_2 and Mg_3Bi_2 by hot-pressing (HP) in the medium temperature range 300–773 K, Kajikawa *et al* estimated a promising dimensionless figure of merit, ZT, for Mg_3Sb_2 of 0.55 at 600 K [1]. In addition, $Ca_xYb_{1-x}Zn_2Sb_2$, which share the same structure as Mg_3Sb_2, have promising ZT values, but lack stability at high temperatures [10].

It is well known that certain impurities and imperfections including deliberate doping drastically affect the electrical properties of a semiconductor [11]. However, the effect of isoelectronic dopants remains unclear, except a modification of the structure with the change in the lattice constant. It

[1] Author to whom any correspondence should be addressed.

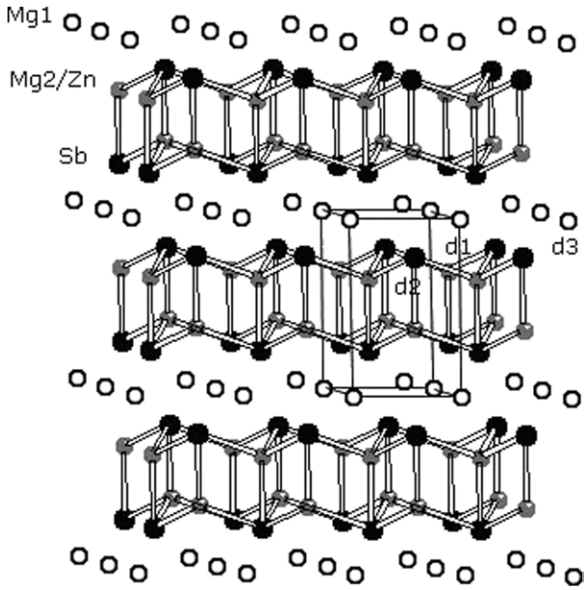

Figure 1. Structure of $(Mg_{1-x}Zn_x)_3Sb_2$ showing the bonding in the Mg/Zn-Sb layer and the separate layer for Mg cations (Mg (label Mg1) hollow, Mg/Zn (label Mg_2/Zn) grey, Sb in black). Unit cell is outlined. The atom distance is marked.

will be interesting to study the influence of an isovalent substitution [12, 13]. The content of Zn substitution on the Mg site in Mg_3Sb_2 can reach 46 at% [14]. $(Mg_{0.62}Zn_{0.38})_3Sb_2$ solid solution has been shown in PDF Nos 04-0849 and 89-4269. Single crystals of magnesium zinc di-antimony, $Mg_{1.59(1)}Zn_{1.41(1)}Sb_2$, were grown by a reaction of elemental Mg, Zn and Sb in an excess of Zn acting as a flux [15]. The compound crystallizes with the trigonal anti-La_2O_3 type (Pearson code hP5). The structure can be regarded as a substitutional derivative of Mg_3Sb_2 by replacing some of the Mg atoms in the tetrahedral position (site symmetry 3m) with Zn atoms, see figure 1. $Mg_{3-x}Zn_xSb_2$ phases with $x = 0$–1.34 were prepared by direct reactions of the elements in tantalum tubes [16]. The thermoelectric performance for two members of the series, Mg_3Sb_2 and $Mg_{2.36}Zn_{0.64}Sb_2$, was evaluated from low to room temperatures through resistivity, Seebeck coefficient and thermal conductivity measurements. In contrast to Mg_3Sb_2, which is a semiconductor, $Mg_{2.36}Zn_{0.64}Sb_2$ is metallic and exhibits an 18 times larger dimensionless figure of merit, ZT, at room temperature. However, it is noted that a secondary phase was detected in all samples except one, and thermoelectric properties were not reported for other samples in $Mg_{3-x}Zn_xSb_2$ except Mg_3Sb_2 and $Mg_{2.36}Zn_{0.64}Sb_2$ by Ahmadpour *et al* [16]. In addition, as pointed out by Ahmadpour *et al* [16], it may still be possible to achieve Zn-richer phases, but this may require changes in the preparation procedures. In other words, to our knowledge, fabricating nanocrystalline $(Mg_{1-x}Zn_x)_3Sb_2$ and its transport properties has seldom been reported so far.

Nanocrystalline materials are polycrystalline materials with grain sizes of up to 100 nm. Because of the extremely small dimensions, a large volume fraction of the atoms is located at grain boundaries, which will give rise to novel or improved physical, mechanical and magnetic properties as compared with those of conventional coarse-grained polycrystalline materials [17]. Mechanical alloying (MA) is capable of producing true alloys from elements that are either not easy to form by conventional means or sometimes even impossible to prepare, e.g. elements which are immiscible under equilibrium conditions. Investigations have revealed that metastable phases, such as supersaturated solid solutions, non-equilibrium crystalline or quasicrystalline, intermediate phases and amorphous alloys, can be synthesized by MA [17]. The prominent observation for MA of binary immiscible systems is the very large metastable solid solubilities that are attained [18]. Nanocrystalline Mg_3Sb_2 has been prepared with high supersaturated solid solubility by MA [19, 20].

The aim of this work was to prepare nanocrystalline $(Mg_{1-x}Zn_x)_3Sb_2$ with high solubility by the method of MA plus HP, which are characterized by both microstructural analyses and electrical resistivity, Seebeck coefficient, thermal conductivity and carrier concentration measurements.

2. Experimental procedure

Powder mixtures of Mg (99%, 100–200 mesh), Sb (99.9%, 200 mesh) and Zn (99%, 200 mesh) with corresponding nominal compositions were filled into a stainless steel vessel (500 ml) along with a certain amount of toluene (100–150 ml). The nominal compositions of the raw mixtures for preparing $(Mg_{1-x}Zn_x)_3Sb_2$ samples studied in this work are presented in table 1. MA was carried out in a high-energy planetary mill (QM-SB) with a speed of 255 r min^{-1} in an Ar atmosphere. A mixture of zirconia grinding balls with different sizes of 10 and 20 mm diameter was used. The ratio of the weight of the balls to the powders (BPR) was 55 : 1 and the number ratio of the large (20 mm in diameter) to the small (10 mm in diameter) balls was 1 : 3. Powder mixtures with the weight of 7–8 g were processed in every milling for 30 h. To obtain bulk samples, as-milled powders were hot-pressed in vacuum under a uni-axial pressure of 300 MPa at 573 K for 60 min. Phase identification was carried out by x-ray diffraction (XRD) (Philips-X'PERT PRO diffractometer) with Cu K_α radiation. The lattice strain and the grain size were estimated based on line broadening of reflection peaks in XRD patterns according to the following equation [17]:

$$b\cos\theta_{bra} = \frac{0.9\lambda_{diff}}{d_{grain}} + \eta\sin\theta_{bra}, \qquad (1)$$

where d_{grain} is the grain size, λ_{diff} the wavelength of the x-ray radiation used, b is the peak width at the half maximum, θ_{bra} is the Bragg angle and η is the lattice strain. Rietveld structure refinement was performed using the GSAS program [21, 22]. Field emission scanning electron microscopy (FE-SEM, SIRION 200) and energy dispersive spectroscopy (EDS, Oxford INCA-energy x-ray microanalysis system) were employed to observe microstructures and to analyse compositions. The actual compositions of bulk samples can be expressed as $(Mg_{1-x}Zn_x)_3Sb_{2+y}$ shown in table 1. The measurements of transport properties (dc resistivity, thermal conductivity and Seebeck coefficient) were carried out on a physical property measurement system (Quantum Design)

Table 1. Various parameters determined for the $(Mg_{1-x}Zn_x)_3Sb_{2+y}$ system: nominal composition, content x and y determined by EDS and Rietveld composition.

		$(Mg_{1-x}Zn_x)_3Sb_{2+y}$		
Sample	Nominal composition	x	y	Refinement composition
S0	Mg62Sb38	0	0.01	$Mg0.92(2)Mg_2Sb_2$
S1	(Mg0.9Zn0.1)62Sb38	0.1	0.01	Mg0.94(3)Mg1.71(2)Zn0.29(2)Sb2
S2	(Mg0.8Zn0.2)62Sb38	0.2	−0.07	Mg0.94(3)Mg1.42(3)Zn0.58(3)Sb2
S3	(Mg0.7Zn0.3)62Sb38	0.32	0.03	Mg0.94(3)Mg1.10(3)Zn0.90(3)Sb2
S4	(Mg0.62Zn0.38)62Sb38	0.39	0	Mg0.97(3)Mg0.89(3)Zn1.11(3)Sb2
S5	(Mg0.55Zn0.45)62Sb38	0.45	−0.06	Mg0.94(3)Mg0.66(3)Zn1.34(3)Sb2
S6	(Mg0.5Zn0.5)62Sb38	0.48	−0.08	Mg0.96(3)Mg0.51(3)Zn1.49(3)Sb2
S7	(Mg0.45Zn0.55)62Sb38	0.55	−0.05	Mg0.92(3)Mg0.34(2)Zn1.66(2)Sb2
S8	(Mg0.4Zn0.6)62Sb38	0.61	0.01	

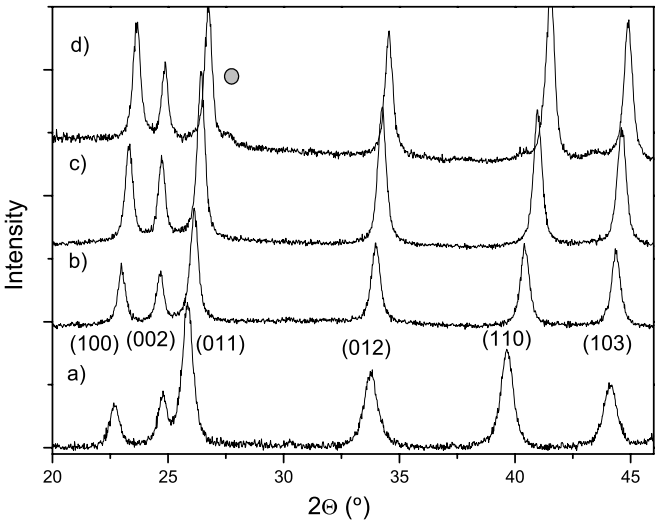

Figure 2. XRD patterns of bulk samples: (a) $x = 0$, (b) $x = 0.32$, (c) $x = 0.45$ and (d) $x = 0.61$.

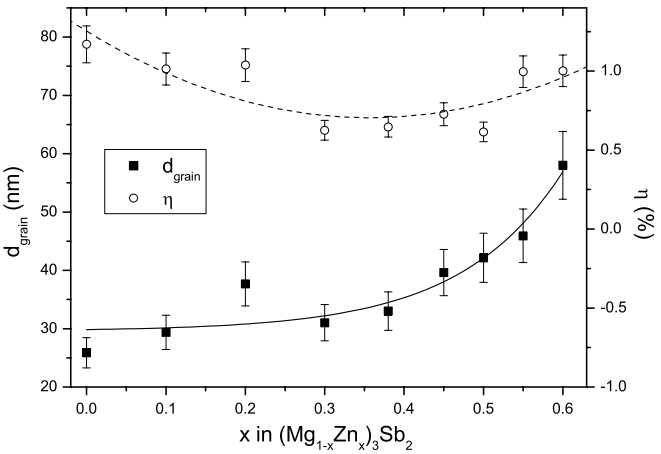

Figure 3. Evolution of the lattice strain (η) and the mean grain size (d_{grain}) of $(Mg_{1-x}Zn_x)_3Sb_2$ with the increasing Zn content (x). Solid lines are a guide to the eye.

(QD-PPMS instrument) below 350 K. Due to the limitation of the maximum electrical resistance measured by PPMS, the low temperature electrical resistivity for the samples $x = 0$ and 0.1 were added and checked by the four-probe method below 300 K. The carrier concentration was measured at room temperature.

3. Results and discussions

3.1. Microstructural characterization of $(Mg_{1-x}Zn_x)_3Sb_{2+y}$ samples

In table 1, various parameters are determined for the $(Mg_{1-x}Zn_x)_3Sb_{2+y}$ system: nominal composition, content x and y determined by EDS and Rietveld composition. One can see that the absolute value of y in $(Mg_{1-x}Zn_x)_3Sb_{2+y}$ is $<\sim 0.08$ in all the bulk samples. This shows that the chemical components of samples S0–S7 are almost stoichiometric. The value of y may be omitted in the following discussion. No obvious elemental precipitation and no trace of impurity elements such as Fe, Ni and Zr are detected by EDS. But a small quantity of oxygen is found in the bulk samples.

Figure 2 shows XRD patterns of the bulk samples with composition x. One can see from curve (a) of figure 2 that the sample S0 ($x = 0$) possesses the same crystallographic structure as that of conventional polycrystalline Mg_3Sb_2 as indexed in the figure, indicating that the monolithic Mg_3Sb_2 phase has been obtained by mechanical milling plus HP. It can be found that there is a systematic shift of the diffraction peaks of Mg_3Sb_2 ($x = 0$) towards a higher angle with increasing Zn content as seen in figures 2(a)–(d). Compared with [16], the phase keeps single until $x \sim 0.61$, a tiny impurity phase is observed on XRD patterns as shown in figure 2(d). However, the secondary phases could be found in all samples except $Mg_{2.2}Zn_{0.8}Sb_2$ prepared by Ahmadpour *et al* [16].

In addition, one can find from figure 2 that the diffraction peaks for all the samples broaden substantially. It can be caused by both grain size and lattice strain. The lattice strain broadening can be caused by any type of lattice defect such as vacancies, interstitials, substitutions and stacking faults [17]. Figure 3 gives the lattice strain and the mean grain size of $(Mg_{1-x}Zn_x)_3Sb_2$ as a function of the Zn content x. The mean grain size increases with exponential growth form from $\sim$25 nm for $x = 0$ to $\sim$55 nm for $x = 0.61$. In contrast to the behaviour of the grain size, the evolution of the lattice strain shows approximately parabolic behaviour from $\sim$1.2% for $x = 0$ to $\sim$0.6% for $x = 0.32$ then to $\sim$1% for $x = 0.61$. To confirm this result, FE-SEM observations were carried out on fracture surfaces of the samples. As

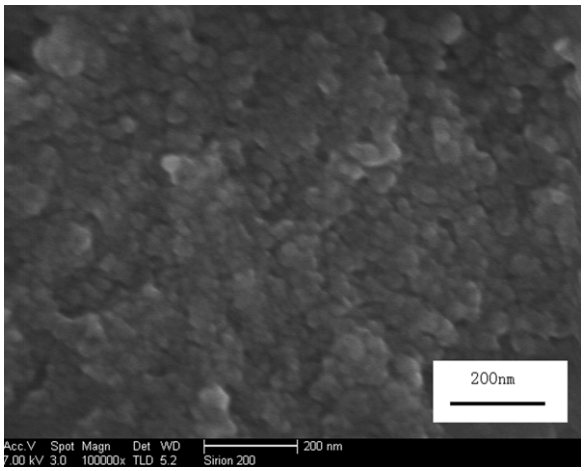

Figure 4. SEM micrograph of the bulk sample $(Mg_{1-x}Zn_x)_3Sb_2$ for $x = 0.55$.

an example, figure 4 gives FE-SEM micrographs of particle (grain) morphologies for $(Mg_{1-x}Zn_x)_3Sb_2$ ($x = 0.55$). It can be seen that particles (grains) of $(Mg_{1-x}Zn_x)_3Sb_2$ are fairly homogeneous and most of them have sizes in the range 30–50 nm, basically in agreement with the XRD results. It may be noted that the mean grain size ~35 nm for $x = 0.2$ is larger than that for $x = 0.1$ and 0.32 in figure 3. It probably affects the transport properties of samples.

Figure 5 shows the evolution of the hexagonal-lattice constants a, c, the volume V of the unit cell, the position parameter z/c for Mg/Zn and Sb in the tetrahedral position (site symmetry 3m), the angle θ of Mg_2–Sb–Mg_2, the nearest distance d_{Mg-Mg} between Mg/Zn and Mg/Zn atoms in the tetrahedral position (site symmetry 3m), the nearest distance d between Mg–Sb and the Zn substitution concentration (SC) on Mg atom in the tetrahedral position (site symmetry 3m) determined by EDS (hypothesizing that the occupied factor of Mg atoms occupying the octahedral position is 1) and the Rietveld structure refinement with zinc content x for $(Mg_{1-x}Zn_x)_3Sb_2$, respectively. With increasing isovalent Zn substitution, the lattice constants a and c decrease linearly monotonically from 4.5602/7.2345 Å for Mg_3Sb_2 to 4.3612/7.1818 Å for $x = 0.61$ in $(Mg_{1-x}Zn_x)_3Sb_2$, as shown in figure 5(a). This result shows that the variation of the lattice parameter with concentration x follows Vegard's law. The lattice constants for Mg_3Sb_2 as reported in [23] are 4.568 and 7.229 Å. The difference between the sample S0 and the reference is because the octahedral position has some vacancy, the occupied factor of Mg is lower than 1, as shown in table 1. Compared with [15, 16, 23], the values and the evolution of the lattice constant a are coincident with the change in the content x. However, the values of the lattice constant c are appreciably higher than the reference. It can be found that the results by Ahmadpour *et al* do not follow Vegard's law especially for the refinement content $Mg_{2.36(2)}Zn_{0.64(2)}Sb_2$, and $Mg_{1.66(2)}Zn_{1.34(2)}Sb_2$ [16]. It can be hypothesized that the refinement results were affected by the secondary phase in the samples of Ahmadpour *et al*. It is easy to understand that the result reported by Xia, etc is lower than nanocrystalline due to XRD at 120 K and the lattice would shrink. Therefore, the volume V of the unit cell also decreases with increasing x and is a little higher than some results reported by Ahmadpour *et al* [16], as shown in figure 5(b). The Sb–Mg distances in the group SbMg7 are not all equal in figure 1 [23], the Mg_2–Sb $d1$ distances decrease from 2.8028 Å for Mg_3Sb_2 to 2.7014 Å for $x = 0.55$, and the Mg(2′)-Sb $d2$ distances decrease from 2.939 Å for Mg_3Sb_2 to 2.8338 Å for $x = 0.55$, the Mg–Sb $d3$ distances decrease from 3.1161 Å for Mg_3Sb_2 to 3.0346 Å for $x = 0.55$, in figure 5(d). The parameter z/c for Mg/Zn in the tetrahedral position decreases slightly with x, but increases with x for Sb. The angle θ of Mg_2–Sb–Mg_2 changes non-monotonically with x. θ decreases till $x = 0.48$, then increases abruptly at $x = 0.55$. At the same time, the distance d_{Mg-Mg} also decreases with increasing x from ~3.293 Å for Mg_3Sb_2 to 3.131 Å for $x = 0.48$ in $(Mg_{1-x}Zn_x)_3Sb_2$ then keeps stable to $x = 0.55$. The solid solution of Zn in nanocrystalline $(Mg_{1-x}Zn_x)_3Sb_2$ detected by EDS has been increased from 0.38 mol% or ~0.45 mol% to ~0.60 mol% compared with coarse crystalline [14, 16]. The Zn SC on Mg atom in the tetrahedral position (site symmetry 3m) determined by Rietveld structure refinement can reach about ~83% at $x = 0.55$ for $(Mg_{1-x}Zn_x)_3Sb_2$ because Mg on the octahedral position is not replaced by Zn and the octahedral Mg position is not disordered. This indicates that the MA process is capable of increasing the solid solution concentration of Zn in $(Mg_{1-x}Zn_x)_3Sb_2$ and obtained the nanocrystalline single phase, compared with the quenching process [16]. Therefore, the lattice strain increases with the supersaturated solid solution concentration as shown in figure 3.

3.2. *Thermoelectric properties of* $(Mg_{1-x}Zn_x)_3Sb_2$

Electrical resistivity ρ, Seebeck coefficient α, the thermoelectric power factor (α^2/ρ) and carrier concentration p at room temperature with different compositions x in $(Mg_{1-x}Zn_x)_3Sb_2$ are listed in table 2. It can be seen that ρ of $(Mg_{1-x}Zn_x)_3Sb_2$ decreases with increasing x from 326 Ω cm for $x = 0$ to 0.0093 Ω cm for $x = 0.55$. The Seebeck coefficient and carrier of $(Mg_{1-x}Zn_x)_3Sb_2$ is positive, indicating that the major charge carriers in $(Mg_{1-x}Zn_x)_3Sb_2$ are holes. The Seebeck coefficients of $(Mg_{1-x}Zn_x)_3Sb_2$ increase with increase in x from 661 μV K^{-1} for $x = 0$ to 717 μV K^{-1} for $x = 0.1$, then decrease to 80 μV K^{-1} for $x = 0.55$, the thermoelectric power factor (S^2/ρ) increases correspondingly from 1.3×10^{-3} μW cm^{-1} K^{-2} for $x = 0$ to 0.688 μW cm^{-1} K^{-2} for $x = 0.55$, ~500 times, and the carrier concentration p increases correspondingly with increasing x from $\sim6\times10^{14}$ cm^{-3} for $x = 0$ to 3×10^{20} cm^{-3} for $x = 0.55$.

Figure 6 shows variation of electrical resistivity for typical samples of $(Mg_{1-x}Zn_x)_3Sb_2$ ($x = 0$, 0.1, 0.32, 0.39, 0.45 and 0.55). It can be seen that as compared with Mg_3Sb_2 ($x = 0$), the resistivity of solid solutions $(Mg_{1-x}Zn_x)_3Sb_2$ decreases systemically with increasing Zn substitution in the entire temperature range investigated. In particular, the temperature behaviour of the solid solution was strongly affected by Zn substitution. In other words, the temperature behaviour of the resistivity for solid solutions $(Mg_{1-x}Zn_x)_3Sb_2$ is different

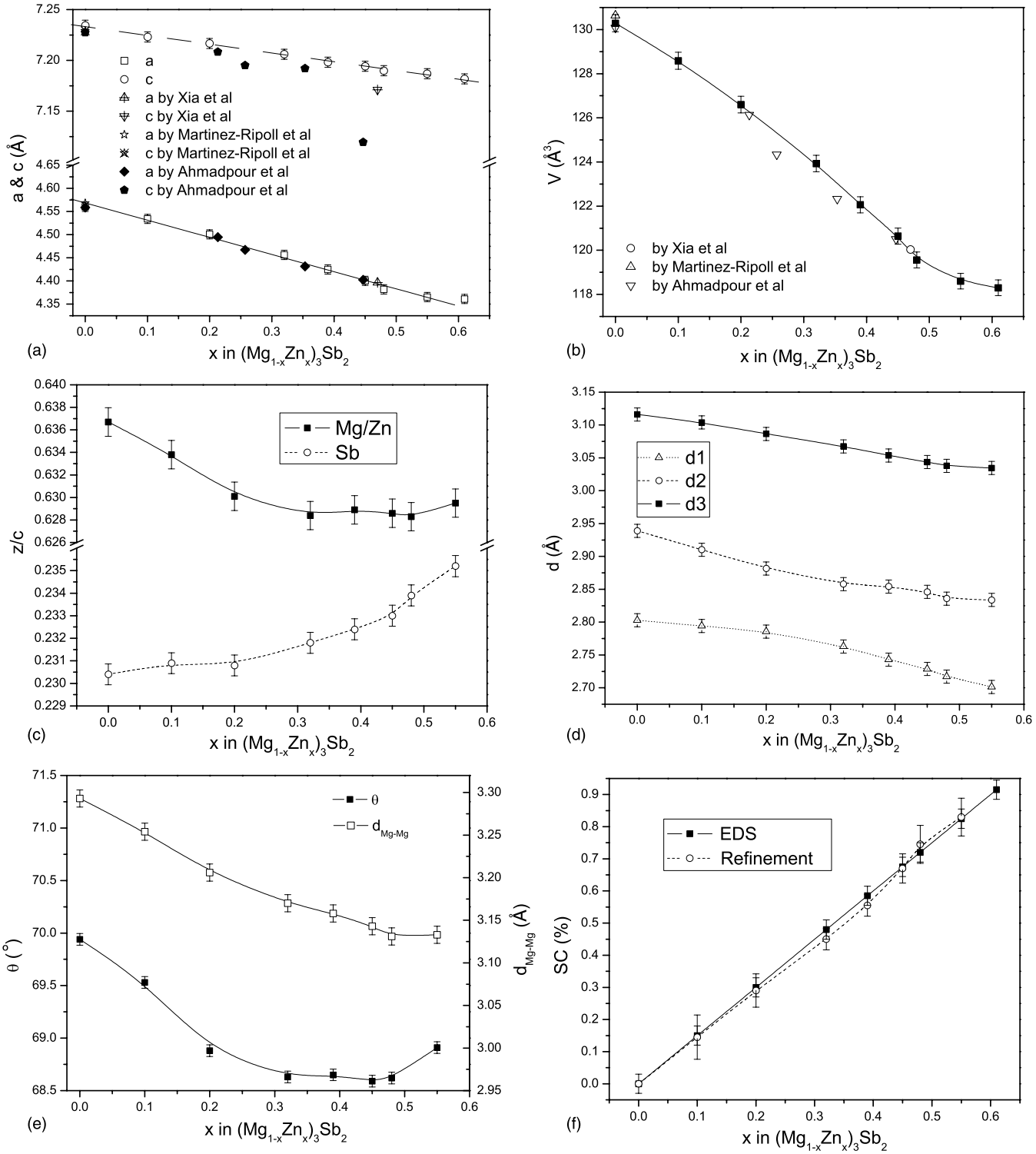

Figure 5. Zinc content x dependence of (a) lattice parameters a, c; (b) volume of unit cell V; (c) position parameter z/c for the tetrahedral position (site symmetry 3m); (d) the nearest distance d between Mg and Sb; (e) the angle θ of Mg_2–Sb–Mg_2 and the nearest distance d_{Mg-Mg} between Mg/Zn and Mg/Zn atoms in the tetrahedral position (site symmetry 3m) and (f) the Zn substitution concentration, SC, on Mg atom in the tetrahedral position (site symmetry 3m) determined by EDS (hypothesizing that the occupied factor of Mg atoms occupying the octahedral position is 1) and Rietveld structure refinement for $(Mg_{1-x}Zn_x)_3Sb_{2+y}$ at room temperature. Some results of the literature are also shown in this figure.

from Mg_3Sb_2, and changes with increasing Zn content. The resistivity decreases with temperature for $x = 0$ and 0.1, decreases slowly for $x = 0.2$ and 0.3, then for more zinc contents $x = 0.45$ and 0.55, it increases with temperature in the medium temperature range. The temperature dependences of the resistivity are typical of heavily doped semiconductors. There is a linear relationship between $\ln \rho$ and $1/T$ only for Mg_3Sb_2 in the high-temperature range measured; for the rest

Table 2. Electrical properties of electrical resistivity ρ, Seebeck coefficient α, thermoelectric power factor α^2/ρ, carrier concentration p and the activation energy E_a with different compositions x in $(Mg_{1-x}Zn_x)_3Sb_2$. The results of Ahmadpour *et al* [16] are shown in parentheses.

x	ρ (300 K) (Ω cm)	α (300 K) (μV K^{-1})	α^2/ρ (300 K) (μW cm^{-1} K^{-2})	p (300 K) (cm^{-3})	E_a (eV)
0	326(3.3)	661(363)	0.0013	6×10^{14}	0.26(0.18)
0.1	143	717	0.0036	6×10^{16}	0.24
0.2	3.17	468	0.0691	5×10^{17}	
(0.21)	(0.216)	(298)			
0.32	0.188	200	0.2128	2×10^{18}	
0.39	0.0569	143	0.3594	1×10^{19}	
0.45	0.0238	104	0.4545	3×10^{19}	
0.55	0.0093	80	0.6882	3×10^{20}	

of the samples this kind of linear relationship holds only in the limited high-temperature regime in figure 6, which is like disorder semiconductor behaviour. Obviously, this linear behaviour (at high temperatures) can be expressed in a thermally activated form as follows [20]:

$$\rho = \rho_0 \exp\left(\frac{E_a}{kT}\right), \tag{2}$$

where ρ_0 is a constant, k is the Boltzmann constant, E_a is the apparent activation energy for conduction. By best fitting of formula (2) to experimental data one obtains the apparent activation energy E_a for Mg_3Sb_2 ($x = 0$) and $x = 0.1$, as listed in table 2. One can see that E_a of nano-$(Mg_{1-x}Zn_x)_3Sb_2$ decreases from 0.26 eV ($x = 0$) to 0.24 eV ($x = 0.1$). It shows that the sample of Mg_3Sb_2 ($x = 0$) is an extrinsic semiconductor [20].

At low temperature, however, the temperature dependences of their resistivity for the samples with $x = 0$ and 0.1 were found to follow Mott's $\ln\rho \propto T^{-1/4}$ law below 180 K, as shown in figure 6(*b*), implying that variable range hopping conduction occurs in these samples. In a disorder semiconductor with partial localization of the carriers, the electron conduction is essentially composed of two forms: (1) thermal excitation of the carriers present in localized state below the mobility edge E_M into extended or delocalized states above E_M and (2) hopping or tunnelling between the localized states around the Fermi level E_F [20]. At relatively high temperatures, the phonon energy will be very high as compared with the energy gap between the nearest neighbour states at E_F. The magnitudes of E_a reflect the energy differences between mobility edge E_M and Fermi level E_F. Obviously, the decrease in E_a with increasing composition x would indicate that the energy difference between the mobility edge and the Fermi level has become small. In the low temperature regions, hopping conduction between the localized states near the Fermi level dominates the conduction process in these specimens. The disorder semiconductor (noncrystalline) phenomenon could be attributed to the Mg vacancies (as determined by refinement), nanocrystalline grain boundaries and the disorder of Mg and Zn atoms in the tetrahedral positions for $(Mg_{1-x}Zn_x)_3Sb_2$.

It can be seen that the peak position is at the temperature of ~263 K for $x = 0.45$ in figure 6(*a*), but it does not move towards the higher temperature; instead it moves contrarily towards the lower temperature of ~180 K for $x = 0.55$ in figure 6. This suggests that the mechanism of the excitation of charge carriers changes due to the electrical structure changes. It is coincident with the change in the angle θ of Mg_2–Sb–Mg_2 increasing abruptly at $x = 0.55$ in figure 5. The atom distances $d1$ and $d2$ of Mg–Sb decrease with increasing zinc content, the angle θ decreases with increasing Zn content up to $x = 0.48$, the distance d_{Mg-Mg} between the Mg/Zn and Mg/Zn atoms in the tetrahedral position (site symmetry 3m) also decreases with increasing x from ~3.293 Å for Mg_3Sb_2 to 3.131 Å for $x = 0.48$ in $(Mg_{1-x}Zn_x)_3Sb_2$ in figure 5. This means that Coulomb repulsion should be increased between Mg/Zn and Mg/Zn atoms in the tetrahedral position with the closer contact, although the electro-negativity difference between the Mg/Zn and the antimony atoms is decreased with increasing zinc content [8]. When Zn substitution concentration is high enough ($x = 0.48$), d_{Mg-Mg} tends to a constant minimum value (see figure 5(*e*)) due to Coulomb repulsion between Mg/Zn and Mg/Zn atoms in the tetrahedral position. Under this condition, increase in substitution concentration ($x > 0.48$) will lead to an increase in angle θ (see figure 5(*e*)), for distances $d1$ and $d2$ decreasing monotonically with increasing x.

The Seebeck coefficient α decreases in the measuring temperature range with increasing x except for the content $x = 0.1$ in figure 7. The curves in figure 7 show noncrystalline/disorder semiconductor behaviour for $x = 0$, 0.1 and 0.2, metal behaviour for $x = 0.32$, 0.45 and 0.55. The noncrystalline/disorder semiconductor behaviour is due to very small sizes of crystallites, about 30–50 nm, and due to disorder. The Mg and Zn atoms randomly occupy the tetrahedral position in the lattice. Below 180 K, the Seebeck coefficients are very small due to hopping conduction (transport) between the localized states around the Fermi level E_F. The hopping conduction between the localized states near the Fermi level dominates the conduction process in these samples. This has been shown in figure 6(*b*). The temperature dependence of the Seebeck coefficient shows that the metallic character increases with increasing the zinc content. The Seebeck coefficient for $x = 0$ is lower than $x = 0.1$ in the measured temperature range. The stoichiometric $CaAl_2Si_2$ structure compound consists of interspersed $Al_2Si_2^{2-}$ layers and Ca^{2+} cation layers. The interactions between the cations and the anionic layers are predominantly ionic and should contribute very little to the energy [9]. The cation layers are considered as electron donors, assign extra electrons into the host $Al_2Si_2^{2-}$ layers. Mg_3Sb_2 compound belongs to the $CaAl_2Si_2$ structure. When there

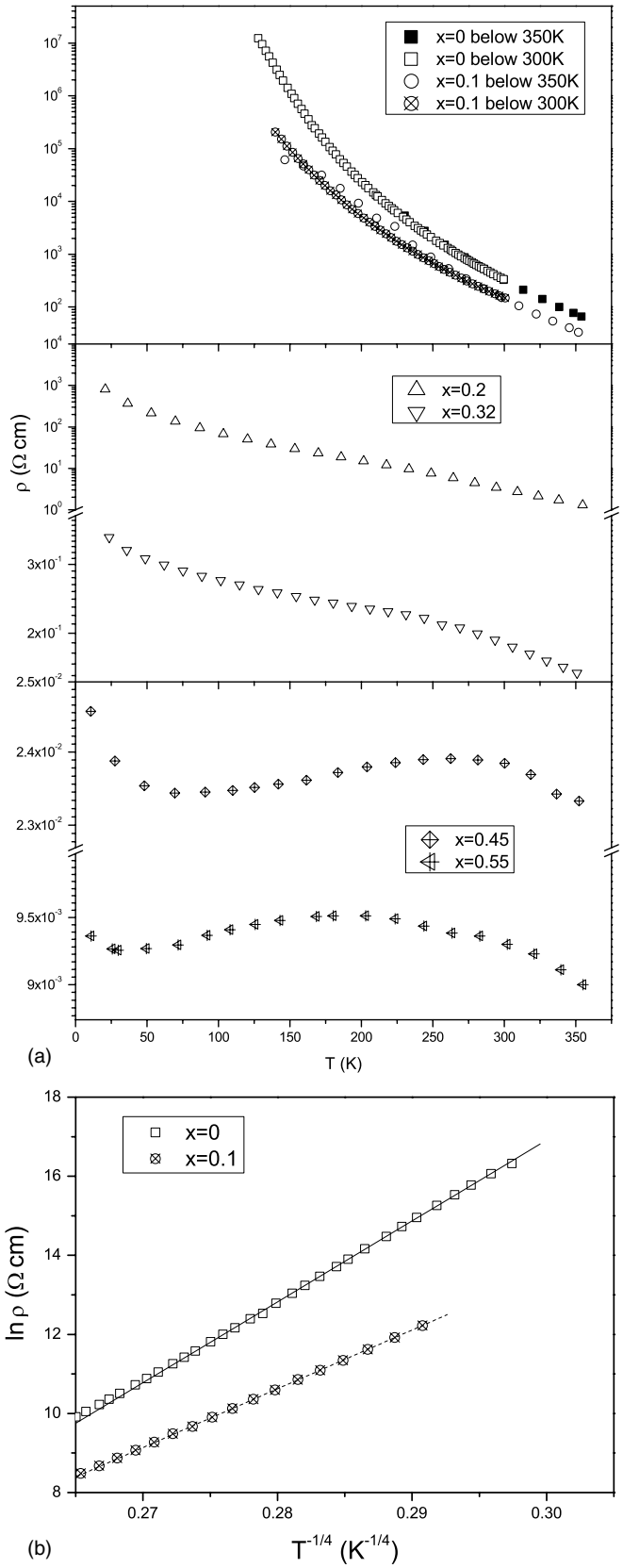

Figure 6. Dependence of the dc electric resistivity ρ on temperature for typical $(Mg_{1-x}Zn_x)_3Sb_2$ samples: (*a*) plot of resistivity ρ versus temperature for $x = 0$, 0.1, 0.2, 0.32, 0.45 and 0.55; (*b*) plot of ln ρ versus $T^{-1/4}$ for $x = 0$ and 0.1.

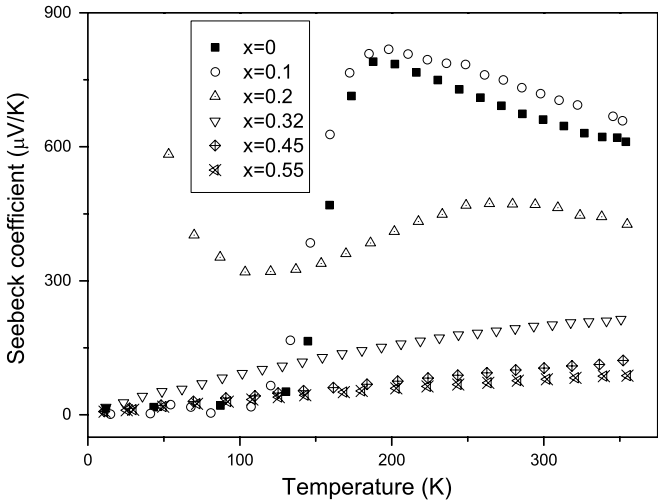

Figure 7. Dependence of the Seebeck coefficient α on temperature for typical $(Mg_{1-x}Zn_x)_3Sb_2$ sample: $x = 0$, $x = 0.1$, $x = 0.2$, $x = 0.32$, $x = 0.45$ and $x = 0.55$.

are some vacancies in the octahedral sites of the lattice, the cation/magnesium layers, the ionicity should be decreased in the Mg_3Sb_2 structure. The results of Rietveld structure refinement show that the occupied factor of Mg is lower than 1 in the octahedral site and the factor of sample S1 is higher than sample S0, as shown in table 1. Therefore, it can be speculated that the ionicity of the S0 sample is lower than S1. The tiny difference of the occupied factor of all samples is due to the preparation procedures.

In theory, the substitution Zn for Mg in $(Mg_{1-x}Zn_x)_3Sb_2$ could not supply more electrons or holes. However, the electrical resistivity ρ, the apparent activation energy E_a, Seebeck coefficient α decreasing and the carrier concentration p increasing indicate that the metallicity increases with increasing correspondingly isovalent zinc SC on Mg in $(Mg_{1-x}Zn_x)_3Sb_2$. This is in accordance with the electric structure calculation results for Mg_3Sb_2 and Mg_2ZnSb_2 by Ahmadpour *et al* [16]. The density of states for Mg_3Sb_2 ($x = 0$) exhibits a band gap and it is expected to be a semiconductor. In Mg_2ZnSb_2, the band gap is closed and the phase should be metallic [16].

Thermal conductivity has two components: the first, the electronic component, depends only on the electrical conductivity σ, according to the Wiedemann–Franz law $\lambda_{el} = L\sigma T$ (the Lorenz number $L = \pi^2 k_B^2/3e^2$), whereas the second, the lattice component λ_L, can be modified by structural disorder. As a rule, an increase in the impurity concentration in the solid solution range leads to a decrease in the lattice thermal conductivity due to phonon scattering by impurity atoms. The temperature dependence of thermal conductivity λ and the lattice thermal conductivity λ_L of the $(Mg_{1-x}Zn_x)_3Sb_2$ system are presented in figure 8. As can be seen from this figure, the Zn concentration dependence of λ_L exhibits a exponential growth character and an anomalous increase is observed in the concentration range $x = 0.10$–0.2 in figure 8(*c*) as in the case of the mean grain size in $(Mg_{1-x}Zn_x)_3Sb_2$ in figure 3. The anomalous increase for $x = 0.2$ may come

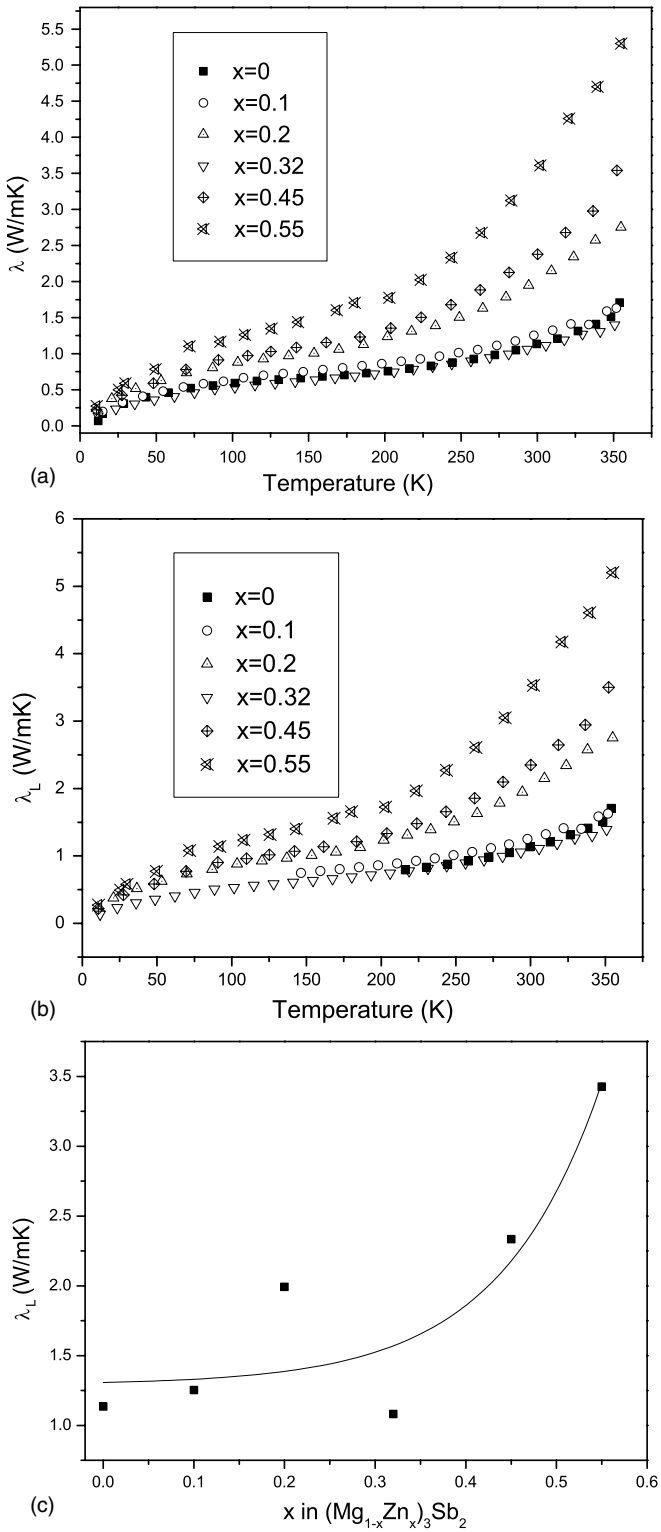

Figure 8. (*a*) Thermal conductivity, (*b*) lattice thermal conductivity of typical $(Mg_{1-x}Zn_x)_3Sb_2$ samples as a function of temperature for $x = 0$, $x = 0.1$, $x = 0.2$, $x = 0.32$, $x = 0.45$ and $x = 0.55$ and (*c*) the concentration x dependences of the lattice conductivity at room temperature for $(Mg_{1-x}Zn_x)_3Sb_2$.

from: (a) grain boundary scattering; due to the small size of the grains, the thermal transport in nanocrystalline materials can be reduced significantly by the strong grain boundary scattering of phonons. That is, the smaller the mean grain size (or the greater the volume fraction of grain boundaries), the stronger the grain boundary scattering is. The mean grain size for $x = 0.2$ is larger than $x = 0.1$ and 0.32 in figure 3. (b) Composition deviation y; the increase in λ_L is related to the remnant Mg or Zn particles, which can be estimated from off-stoichiometry that is characterized by composition deviation y. In particular, y is -0.07, -0.06 and -0.05 for $x = 0.2$, 0.45 and 0.55 in the $(Mg_{1-x}Zn_x)_3Sb_{2+y}$ system. In addition, the occupied factor of the Mg atom in the octahedral site is lower than 1 determined by Rietveld structure refinement. This means that some remnant Mg/Zn particles are kept in $(Mg_{1-x}Zn_x)_3Sb_{2+y}$ samples, which would increase the thermal conductivity of $(Mg_{1-x}Zn_x)_3Sb_2$ solid solutions. The value of λ for the $x = 0.32$ sample is about $1.08\,W\,m^{-1}K^{-1}$ at room temperature, which is lower than for the Mg_3Sb_2 sample (about $1.13\,W\,m^{-1}\,K^{-1}$). The lowest value λ is attributed to grain boundary scattering and the maximum disordered behaviour for $x = 0.32$. The occupied factor for Mg or Zn is very close to 0.5 in the tetrahedral position, which is a consequence of most effective phonon scattering on the mixed Mg/Zn sites [16]. Considering the relative simplicity of the crystal structure, the thermal conductivities are reasonably low and comparable to those of good thermoelectric materials for $x = 0.32$ [10].

Comparing the results with the literature data at room temperature, the Seebeck coefficient of $661\,\mu V\,K^{-1}$ at 300 K, $646\,\mu V\,K^{-1}$ at 310 K and $630\,\mu V\,K^{-1}$ at 330 K for Mg_3Sb_2 sample is larger than the value of $363\,\mu V\,K^{-1}$ reported by Ahmadpour *et al* [16] for 300 K, $\sim 250\,\mu V\,K^{-1}$ reported by Kajikawa *et al* [1] for 330 K and $\sim 25\,\mu V\,K^{-1}$ reported by Condron *et al* [24] for 310 K, but is close to $\sim 620\,\mu V\,K^{-1}$ reported by Boltaks *et al* [25]. The Mg_3Sb_2 sample resistivity of 326 Ω cm is higher than the results reported by [1, 16, 24], but also lower than ∼1200 Ω cm reported by Boltaks *et al* [25]. The value of the thermal conductivity $1.13\,W\,m^{-1}\,K^{-1}$ at room temperature is close to $\sim 1\,W\,m^{-1}\,K^{-1}$ given by Boltaks *et al* [25] but lower than other results reported by other references. The physical properties of $Mg_{2.36}Zn_{0.64}Sb_2$ are reported by Ahmadpour *et al* [16]. The composition is close to $x = 0.2$ for $(Mg_{1-x}Zn_x)_3Sb_2$ solid solutions. The Seebeck coefficient of $468\,\mu V\,K^{-1}$ at 300 K for the $x = 0.2$ sample is larger than the value of $298\,\mu V\,K^{-1}$ reported by Ahmadpour *et al* [16]. The resistivity of 3.17 Ω cm is higher than the result of 0.216 Ω cm reported by Ahmadpour *et al* [16]. The value of the thermal conductivity $2\,W\,m^{-1}K^{-1}$ at room temperature is larger than the value of $1.16\,W\,m^{-1}\,K^{-1}$ given by Ahmadpour *et al* [18]. However, the value $1.08\,W\,m^{-1}\,K^{-1}$ of λ for $x = 0.32$ is lowest in the literature for $(Mg_{1-x}Zn_x)_3Sb_2$. As pointed out by Ahmadpour *et al* and Condron *et al* [24], different preparation techniques are likely to be the cause of different values observed [16]. In brief, for nanocrystalline $(Mg_{1-x}Zn_x)_3Sb_2$, the Seebeck coefficients and the electrical resistivity are higher, the thermal conductivity is lower than the coarse crystalline materials (sintering materials) [16] due to carrier-energy filtering or quantum confinement and grain boundary scattering [26].

The dimensionless figure of merit, $ZT = \alpha^2 T/\rho\lambda$, as a function of temperature for $x = 0$, $x = 0.1$, $x = 0.2$, $x = 0.32$, $x = 0.45$ and $x = 0.55$ in the $(Mg_{1-x}Zn_x)_3Sb_2$

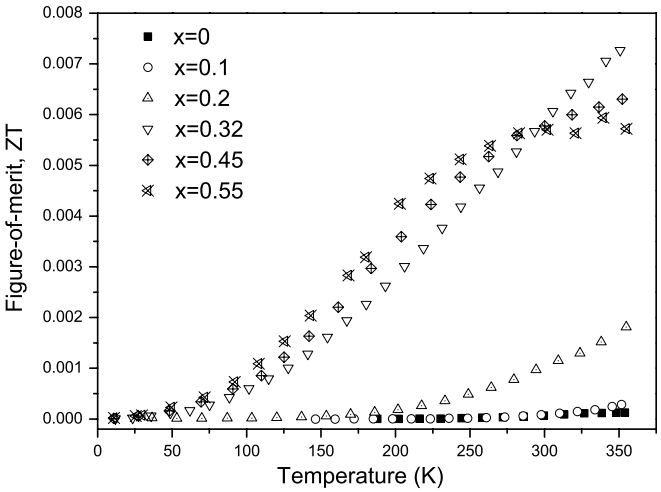

Figure 9. Dimensionless figure of merit, ZT, as a function of temperature for $x = 0$, $x = 0.1$, $x = 0.2$, $x = 0.32$, $x = 0.45$ and $x = 0.55$ in $(Mg_{1-x}Zn_x)_3Sb_2$.

samples is shown in figure 9. ZT for $x = 0.32$, 0.45 and 0.55 at room temperature is almost equivalent, and is over 80 times larger than that for Mg_3Sb_2, which is mostly due to their lower electrical resistivity. The value 7×10^{-3} of ZT for $x = 0.32$ is the largest at 350 K due to its lowest thermal conductivity. Finally, thermoelectric properties of $(Mg_{1-x}Zn_x)_3Sb_2$ can be tuned by isovalent Zn substitution on Mg due to the increasing metallicity with x.

4. Conclusions

In summary, the structure and transport properties can be tuned by the change in x in $(Mg_{1-x}Zn_x)_3Sb_2$ prepared by MA from $x = 0$ to ~0.6. It can be almost 90% concentration by replacing some of the Mg atoms in the tetrahedral position with Zn atoms in $(Mg_{1-x}Zn_x)_3Sb_2$. A full substitution of the Mg atoms in the tetrahedral position by the Zn atoms would be difficult by means of MA. The Coulomb repulsion should be increased between Mg/Zn and Mg/Zn atoms in the tetrahedral position with the closer contact and greater Zn content, the angle θ for Mg–Sb–Mg of the tetrahedral position should be increased to relax the repulsion between the Mg/Zn and Mg/Zn atoms when the distances $d1$ and $d2$ between Mg/Zn and Sb decrease at $x = 0.55$, the distance d_{Mg-Mg} does not decrease. In contrast to Mg_3Sb_2, $(Mg_{1-x}Zn_x)_3Sb_2$ ($x = 0.32$) exhibits an above 80 times larger dimensionless figure of merit, ZT, at room temperature. However, the thermoelectric performance of nanocrystalline $(Mg_{1-x}Zn_x)_3Sb_2$ is still poor and it is mostly due to its large electrical resistivity, although the thermal conductivities (~1.08 $W\,m^{-1}\,K^{-1}$) for $x = 0.32$ are reasonably low and comparable to those of good thermoelectric materials due to more grain boundary scattering than a coarse crystal.

Acknowledgments

Financial support from the National Natural Science Foundation of China (No 50371081), the Natural Science Foundation of Anhui Province (No 070414203) and the Director Foundation of the Institute of Solid State Physics, Chinese Academy of Science (No 074N131145) are gratefully acknowledged.

References

[1] Kajikawa T, Kimura N and Yokoyama T 2003 *22nd Int. Conf. Thermoelectrics (LaGrande Motte, France)* pp 305–8
[2] Honda H, Sakaguchi H, Tanaka I and Esaka T 2003 *J. Power Sources* **123** 216–21
[3] Singh P and Sarkar K K 1985 *Solid State Commun.* **55** 439–42
[4] Nishimiya N, Suzuki A and Ono S 1982 *Int. J. Hydrogen Energy* **7** 741–50
[5] Viala J C, Barbeau F, Bosselet F and Peronnet M 1998 *J. Mater. Sci. Lett.* **17** 757–60
[6] Slowik J H 1974 *Phys. Rev.* B **10** 416–31
[7] Watson L M, Marshall C A W and Cardoso C P 1984 *J. Phys. F: Met. Phys.* **14** 113–21
[8] Zheng C, Hoffmann R, Nesper R and von Schnering H-G 1986 *J. Am. Chem. Soc.* **108** 1876–84
[9] Zheng C and Hoffmann R 1988 *J. Solid State Chem.* **72** 58–71
[10] Gascoin F, Ottensmann S, Stark D, Haïle S M and Jeffrey Snyder G 2005 *Adv. Funct. Mater.* **15** 1860–4
[11] Kittel C 1996 *Introduction to Solid State Physics* 7th edn (New York: Wiley) pp 221–2
[12] Kazakov S M, Angst M, Karpinski J, Fita I M and Puzniak R 2001 *Solid State Commun.* **119** 1–5
[13] Medvedeva N I, Ivanovskii A L, Medvedeva J E and Freeman A J 2001 *Phys. Rev.* B **64** 020502(R)
[14] Landolt-Bornstein 1971 *Numerical Data and Functional Relationships in Science and Technology, New Series, Group: III. Crystal and Solid Physics, vol 6: Structure Data of Elements and Intermetallic Phases* (Berlin: Springer) p 724
[15] Xia S-Q, King P and Bobev S 2006 *Acta Crystallogr. E: Struct. Rep.* **62** i184–i186
[16] Ahmadpour F, Kolodiazhnyi T and Mozharivskyj Y 2007 *J. Solid State Chem.* **180** 2420–8
[17] Suryanarayana C 2001 *Prog. Mater. Sci.* **46** 1–184
[18] Koch C C 1993 *Nanostruct. Mater.* **2** 109–29
[19] Xin H X, Qin X Y, Zhu X G, Zhang J and Kong M G 2006 *Mater. Sci. Eng.* B **128** 192–200
[20] Xin H X, Qin X Y, Zhu X G and Liu Y 2006 *J. Phys. D: Appl. Phys.* **39** 375–81
[21] Toby B H 2001 EXPGUI, a graphical user interface for GSAS *J. Appl. Crystallogr.* **34** 210–21
[22] Larson A C and Von Dreele R B 2004 General Structure Analysis System (GSAS) *Los Alamos National Laboratory Report* LAUR 86-748
[23] Martinez-Ripoli M, Haase A and Brauer G 1974 *Acta Crystallogr.* B **30** 2006–9
[24] Condron C L, Kauzlarich S M, Gascoin F and Snyder G J 2006 *J. Solid State Chem.* **179** 2252–7
[25] Boltaks B I and Zhuze V P 1948 *J. Tech. Phys. (USSR)* **18** 1459–77
[26] Dresselhaus M S *et al* 2007 *Adv. Mater.* **19** 1043–53